

COMMUNICATION

[View Article Online](#)
[View Journal](#) | [View Issue](#)Cite this: *J. Mater. Chem. A*, 2023, **11**, 23233Received 4th August 2023
Accepted 17th October 2023

DOI: 10.1039/d3ta04665f

rsc.li/materials-a

Zirconia-free NaSICON solid electrolyte materials for sodium all-solid-state batteries†

Aaron Jue Kang Tieu,^{‡a} Eunike Mahayoni,^{‡bc} Yuheng Li,^{‡a} Zeyu Deng,^{‡a} François Fauth,^{‡d} Jean-Noël Chotard,^{bc} Vincent Seznec,^{‡bc} Stefan Adams,^{‡*a} Christian Masquelier^{‡*bce} and Pieremanuele Canepa^{‡*afg}

The growing demand for energy storage systems has sparked a race to build inexpensive and safer rechargeable batteries. All-solid-state sodium (Na)-ion batteries are a competitive alternative to their lithium (Li) analogs due to the lower cost of Na resources. The Na Superionic CONductors $\text{Na}_{1+x}\text{Zr}_2\text{Si}_x\text{P}_{3-x}\text{O}_{12}$ ($0 \leq x \leq 3$) (NZSP) are widely studied as solid electrolytes. However, synthesized NZSPs always contain monoclinic ZrO_2 as the main impurity phase, which may lead to a lower Na-ion ionic conductivity within the solid-electrolyte layer. Here, we synthesize zirconia-free NZSP by engineering the quantity of zirconium (Zr) precursors. Synchrotron X-ray diffraction, Raman spectroscopy, and density functional theory simulations reveal zirconia-free NZSP. Impedance spectroscopy measurement of zirconia-free NZSP reveals an impressive total ionic conductivity of $\sim 3.49 \text{ mS cm}^{-1}$ with a bulk conductivity of $\sim 10.05 \text{ mS cm}^{-1}$ at room temperature, making it an excellent Na-ion conductor for all-solid-state batteries. Battery tests of symmetric cells confirm that zirconia-free NZSP electrolyte provides significantly improved performance. These results pave the way towards the synthesis optimization of impurity-free complex solid-electrolytes, which are important if solid-state batteries are to be commercialized.

Introduction

The need to reduce our reliance on carbon-based fossil fuels and the importance of optimizing the process of harvesting intermittent energies, such as wind and solar energy has prompted a surge for suitable energy storage systems that are safe, reliable, and cost-efficient. Although lithium (Li)-ion batteries (LIBs) are considered some of the most promising energy storage systems,¹ their electrolytes consist of Li salts in a mixture of nonaqueous flammable organic solvents,² which pose serious fire hazards³ in the event of thermal runaways. While LIBs share the same working principles as sodium (Na)-ion batteries (NIBs),⁴ NIBs have reduced costs due to sodium's high relative abundance compared to Li (2.5% vs. 0.0032% of Earth's crust).⁵ NIBs use inexpensive aluminum current collectors instead of costly copper ones in LIBs. All-solid-state Na batteries (ASSBs) can eliminate the flammability of liquid electrolytes through their replacement with fast Na solid electrolyte (SE) materials.^{6,7} Within the class of SEs, the Na Superionic CONductor (NaSICON) polyanionic compounds are widely regarded for their high Na-ion conductivity, which can be tuned *via* structural changes of their anionic frameworks.^{8–12} Notably, NaSICONs have been studied as both electrodes^{13–19} and solid electrolytes.^{20–26}

NaSICON-type structures, $\text{Na}_{1+x}\text{Zr}_2\text{Si}_x\text{P}_{3-x}\text{O}_{12}$ ($0 \leq x \leq 3$), hereafter referred to as NZSP, exhibits superior ionic conductivity,^{27,28} with total ionic conductivities approaching $\sim 5 \text{ mS cm}^{-1}$. $\text{Na}_3\text{Zr}_2\text{Si}_2\text{PO}_{12}$ (N3.0ZSP) is widely studied and optimized, *via* doping or materials processing to improve its ionic conductivity for ASSBs. Recent studies have shown that phases with the nominal composition $\text{Na}_{3.4}\text{Zr}_2\text{Si}_{2.4}\text{P}_{0.6}\text{O}_{12}$ (N3.4ZSP) can sustain a higher total ionic conductivity of $\sim 4.5 \text{ mS cm}^{-1}$ and a bulk ionic conductivity of $\sim 11 \text{ mS cm}^{-1}$ at room temperature,^{21,32} making these materials attractive candidates for ASSBs. Increased ionic conductivities in N3.4ZSP (vs. N3.0ZSP) are attributed to the lower migration barriers introduced by the higher Si content and an optimally tuned Na-to-vacancy ratio.³²

^aDepartment of Materials Science and Engineering, National University of Singapore, College of Design and Engineering, 117575, Singapore. E-mail: mseasn@nus.edu.sg

^bLaboratoire de Réactivité et de Chimie des Solides (LRCS), CNRS UMR 7314, Université de Picardie Jules Verne, 80039 Amiens Cedex, France. E-mail: christian.masquelier@u-picardie.fr

^cRS2E, Réseau Français sur le Stockage Electrochimique de l'Energie, FR CNRS 3459, F-80039 Amiens Cedex 1, France

^dCELLS-ALBA Synchrotron, Cerdanyola del Vallès, E-08290 Barcelona, Spain

^eALISTORE-ERI European Research Institute, FR CNRS 3104, F-80039 Amiens Cedex 1, France

^fDepartment of Electrical and Computer Engineering, Houston, TX 77204, USA

^gTexas Center for Superconductivity, University of Houston, Houston, TX, 77204, USA. E-mail: pcanepa@uh.edu

† Electronic supplementary information (ESI) available. See DOI: <https://doi.org/10.1039/d3ta04665f>

‡ These authors contributed equally.

Notwithstanding the significant progress in the optimization of the synthesis processes to obtain dense, highly ionic conductive NZSPs, their synthesis is largely plagued by the presence of grain boundaries (reducing Na^+ conductivity), and most importantly the segregation of impurity phases,^{33–36} in particular, monoclinic zirconia (m-ZrO_2 , with space group $P2_1/c$). The formation of m-ZrO_2 has been largely attributed to the evaporation of Na and phosphorous (P) precursors at elevated sintering temperatures ($>1000^\circ\text{C}$).^{37–40} The m-ZrO_2 forms on the grain boundaries of the NZSP pellet during annealing and can be linked to either inhomogeneous mixing pre-sinterings, or as a result of Na and P losses at the grain boundaries as volatile components. Therefore, by reducing the amount of Zr precursor, the formation of m-ZrO_2 will be controlled as we are working in a Zr-deficient environment. Various attempts have been made to improve the phase purity of NZSPs, either by increasing appropriately the amount of Na and P^{41,42} or by using starting materials with smaller particle sizes to increase the homogeneity of precursors during mixing.^{43,44} Nevertheless, large deviations in the reproducibility of these syntheses were observed,³² which may be linked to the synthesis^{45,46} conditions, and how the NZSP samples are stored^{47–49} before measurements.

The actual composition of NZSP reported has also been debated. Various reports proposed the actual composition of NZSP based on their syntheses,^{50,51} where compositions can vary on sites other than Na, P, and Si. Zr deficient NZSP compositions⁵² have also been proposed, in addition to other possible

compositions arising from the investigation⁵³ of the quaternary phase diagram of $\text{Na}_2\text{O-P}_2\text{O}_5\text{-SiO}_2\text{-ZrO}_2$. Based on existing studies and hypotheses found in the literature, to date, there seems to be no general agreement on a formula describing NaSICONs.⁵³

Here, we show that a suitably tuned synthesis protocol of NZSP can reduce and even eliminate monoclinic m-ZrO_2 . We synthesize NZSP *via* the solution-assisted solid-state reaction (SA-SSR) while varying the amount of our zirconium (Zr) precursor during the initial mixing in the synthesis. The SA-SSR provides a relatively inexpensive and straightforward synthesis protocol, and the control of only the Zr precursor eliminates the problem of the variation in the amount of Na and P to compensate into the initial reaction mixtures that have been reported thus far.^{43,44,54,55} We show that lowering the amount of Zr precursors, specifically $\text{ZrO}(\text{NO}_3)_2 \cdot 3.7\text{H}_2\text{O}$ (up to an optimal value of $\sim 15\%$ less Zr), results in a zirconia-free NZSP crystallizing in the monoclinic space group $C2/c$. These findings are substantiated by synchrotron powder X-ray diffraction (SPXRD), inductively coupled plasma optical emission spectroscopy (ICP-OES), Raman spectroscopy, scanning electron microscopy (SEM), electrochemical impedance spectroscopy (EIS), as well as density functional theory (DFT) calculations. Our results are useful in guiding future research on related polyanion electrolyte materials to achieve phase-pure target compositions, with accurate control of the structure–property relationships of these complex solid electrolytes.

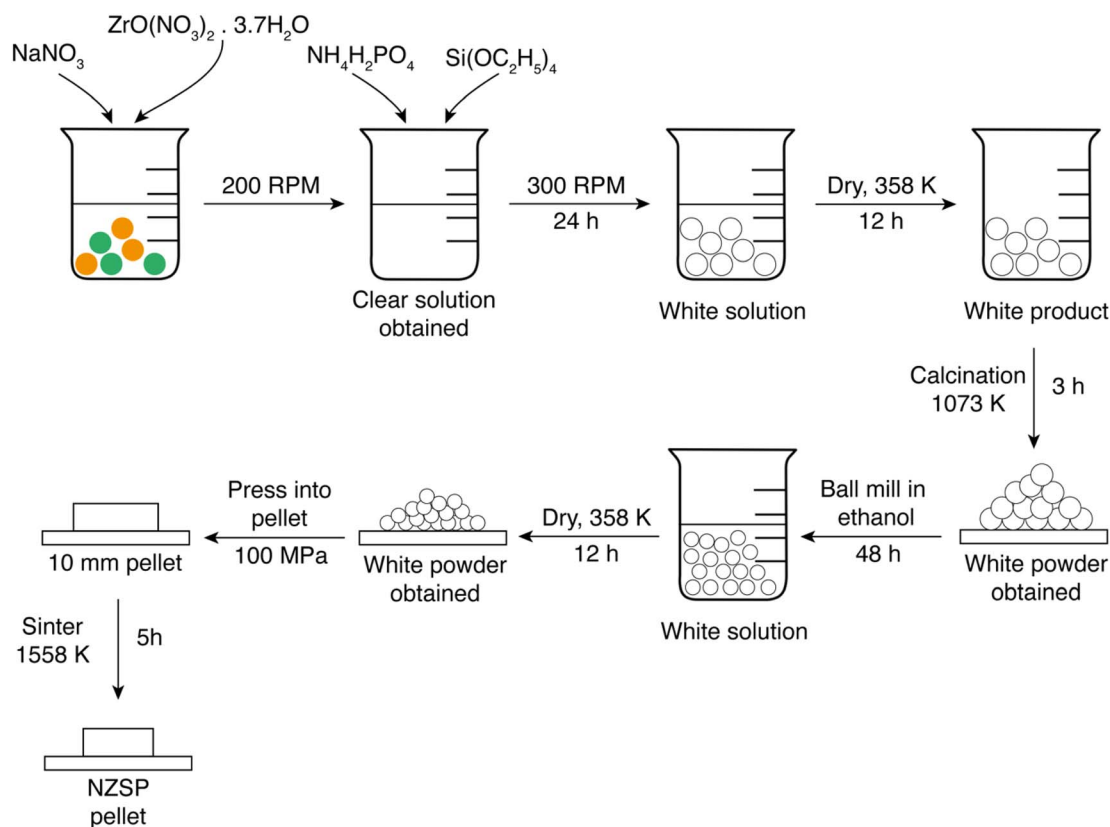


Fig. 1 Synthesis procedure *via* the SA-SSR of all NZSP samples reported in this work.

Results

Samples discussed here are labeled as Lx (where x is the percentage reduction of Zr precursors added). For example, sample L5 means that the NZSP was synthesized by adding 95% of the stoichiometric amount of $\text{ZrO}(\text{NO}_3)_2 \cdot 3.7\text{H}_2\text{O}$ expected (5% less than the original stoichiometric amount).

Fig. 1 shows the SA-SSR for all NZSP samples. Stoichiometric amounts of NaNO_3 ($\geq 99.0\%$, Sigma-Aldrich) and $\text{ZrO}(\text{NO}_3)_2 \cdot 3.7\text{H}_2\text{O}$ (99.9%, Alfa-Aesar) were initially dissolved into deionized water. A stoichiometric amount of $\text{ZrO}(\text{NO}_3)_2 \cdot 3.7\text{H}_2\text{O}$ was determined by thermogravimetric analysis (TGA) (Fig. S1 of ESI†). Once the solution turned clear, a stoichiometric amount of $\text{Si}(\text{OC}_2\text{H}_5)_4$ ($\geq 99.0\%$, Sigma-Aldrich) was added to the solution upon stirring. When $\text{Si}(\text{OC}_2\text{H}_5)_4$ was hydrolyzed, a stoichiometric amount of $\text{NH}_4\text{H}_2\text{PO}_4$ ($\geq 98.5\%$, Sigma-Aldrich) was then added to the solution while stirring, resulting in a milky white solution. The mixture was then mixed for 24 hours while stirring at 300 rpm at room temperature. The product was dried at $\sim 358\text{ K}$ overnight, for 12 hours, with the obtained dried powder subsequently calcined at $\sim 1073\text{ K}$ for 3 hours in air. After calcination, a white powder was obtained, which was subsequently ball-milled at 250 rpm for 48 hours in ethanol with balls and milling jars made of ZrO_2 . The resulting mixture was dried overnight at $\sim 358\text{ K}$ for 12 hours. The powder obtained was cold pressed with a 10 mm pellet die, at 100 MPa of pressure before sintering at 1558 K for 5 hours in the furnace in air.

The weight percentages of Na, Zr, Si, and P to the total weight of the sample (%w/w) were analyzed with ICP-OES (see Table S2 of ESI†). The stoichiometry derived by setting $\text{Si} + \text{P} = 3.0$ of the ratio $\text{Na} : \text{Zr} : \text{Si} : \text{P}$ was found to be $\sim 3.634 : 1.711 : 2.414 : 0.586$ for the L15 sample. This suggests that the $\text{Zr} : (\text{Si} + \text{P})$ ratio in the product is close to the nominal composition of the precursors. Fig. 2a shows the powder X-ray diffraction (PXRD) patterns of several NZSP-Lx samples, which are L0 (–0% $\text{ZrO}(\text{NO}_3)_2 \cdot 3.7\text{H}_2\text{O}$), L5 (–5%), L10 (–10%), L15 (–15%), L20 (–20%), and L25 (–25%). The m- ZrO_2 is marked with *, $\text{Na}_2\text{ZrSi}_2\text{O}_7$ with #, and Na_3PO_4 with & in the PXRD. Rietveld refinements of the PXRDs of Fig. 2a revealed the presence of NZSP and other impurities indexed here, with weight percentages shown in Table S3 of ESI†. Structures used to index these phases in the PXRDs are $\text{Na}_{3.4}\text{Zr}_2\text{Si}_{2.4}\text{P}_{0.6}\text{O}_{12}$ (a modified N3.4ZSP from $C2/c$ N3.0ZSP, ICSD 473), m- ZrO_2 ($P2/c$, ICSD 18190), $\text{Na}_2\text{ZrSi}_2\text{O}_7$ ($P\bar{1}$, ICSD 24866), and Na_3PO_4 ($P4_21c$, ICSD 97205).

With a decreasing amount of Zr precursors from L0 to L15, the amount of m- ZrO_2 impurity progressively decreases and eventually disappears in L15. While m- ZrO_2 could not be detected in samples L20 and L25, in the PXRDs of Fig. 2a we observe signatures of other impurities, such as Na_3PO_4 and $\text{Na}_2\text{ZrSi}_2\text{O}_7$. The zoomed-in figure in Fig. 2b, at angles between 2θ range 27.5° and 32° shows the region where m- ZrO_2 diffraction peaks are identified. The region in Fig. 2b shows a monotonic decrease in the intensity of the m- ZrO_2 peaks as the amount of Zr precursors decreases in the synthesis. Indeed, the extracted ZrO_2 weight fractions in L0 (7.93%), L5 (3.72%), L10 (2.65%), L15 (0%), L20 (0%), and L25 (0%) obtained *via* the

Rietveld refinements of PXRDs (Table S3 in ESI†) confirms that samples L15, L20, and L25 do not contain any trace of crystalline of m- ZrO_2 . Based on our laboratory PXRD results in Fig. 2a and b, the optimal amount of Zr precursor is 15% less $\text{ZrO}(\text{NO}_3)_2 \cdot 3.7\text{H}_2\text{O}$ than the stoichiometric amount, which also avoids the formation of other impurities, *e.g.* Na_3PO_4 and $\text{Na}_2\text{ZrSi}_2\text{O}_7$.

Fig. 2c shows the synchrotron PXRD of L15 (and its associated Rietveld refinement) measured at the synchrotron beamline BL04-MSPD, ALBA, Spain. Albeit with better resolution compared to the PXRD of L15 from our laboratory XRD (Fig. 2a and b), Fig. 2c again does not reveal any of the characteristic Bragg peaks of m- ZrO_2 . The sample L15 crystallizes with a monoclinic ($C2/c$) symmetry, and the lattice constants are $a = 15.7189(4)\text{ \AA}$, $b = 9.0929(2)\text{ \AA}$, $c = 9.2164(2)\text{ \AA}$, $\beta = 124.1905(14)^\circ$ when indexed with a N3.4ZSP crystal structure, in accordance with existing reports for N3.4ZSP.³² Atomic coordinates, U_{iso} values, and other parameters are summarized in Table S4 of the ESI†.

Having established the purity of L15, we performed variable temperature laboratory PXRD measurements (Fig. 2d) to ascertain the phase-transition temperature of the monoclinic ($C2/c$) phase to the high Na-ion conductivity rhombohedral ($R\bar{3}c$) phase, in the 2θ range 10° to 40° and from 303 K to 573 K .

Fig. 2e are insets of Fig. 2d identifying the temperature of the monoclinic (mono) \rightarrow rhombohedral (rhomb) phase transition for L15. Based on Rietveld refinement, the expected reflections are:

- (1) In the monoclinic (mono) phase 2θ angles between $18.6\text{--}19.6^\circ$: $(-2\ 0\ 2)_{\text{mono}}$, $(1\ 1\ 1)_{\text{mono}}$, $(0\ 2\ 0)_{\text{mono}}$, and $(-3\ 1\ 1)_{\text{mono}}$. For the rhombohedral (rhomb) phase: $(1\ 0\ 4)_{\text{rhomb}}$, and $(1\ 1\ 0)_{\text{rhomb}}$.
- (2) In the monoclinic phase 2θ angles between $22\text{--}23^\circ$: $(-3\ 1\ 2)_{\text{mono}}$, $(0\ 2\ 1)_{\text{mono}}$, and $(3\ 1\ 0)_{\text{mono}}$. For the rhombohedral phase: $(1\ 1\ 3)_{\text{rhomb}}$ and $(0\ 0\ 6)_{\text{rhomb}}$.
- (3) In the monoclinic phase 2θ angles between $26.6\text{--}27.8^\circ$: $(-2\ 2\ 2)_{\text{mono}}$ and $(4\ 0\ 0)_{\text{mono}}$. For the rhombohedral phase: $(0\ 2\ 4)_{\text{rhomb}}$.

The expected monoclinic \rightarrow rhombohedral phase-transition temperature for N3.4ZSP takes place at $\sim 414\text{ K}$,³² with peak changes from the monoclinic phase to the rhombohedral phase detected at 2θ angles between $18.6\text{--}19.6^\circ$ (d), $22\text{--}23^\circ$ (e), and $26.6\text{--}27.8^\circ$ (f). In L15, an onset temperature of the phase transition happens at $\sim 403\text{ K}$. DSC measurements of L15 shown in Fig. S6 of ESI† also confirmed an endothermic monoclinic \rightarrow rhombohedral transformation at $\sim 396.5\text{ K}$. The slight reduction of the transition temperature might suggest a slightly higher Na content in our sample.^{29–32}

We employed Raman spectroscopy to: (i) clarify whether our samples contain impurity phases, or possible amorphous phases that would be undetectable by PXRDs, and (ii) ascertain the structural moieties present in these NZSP phases. Fig. 3 depicts the Raman spectra of several NZSP samples (L0, L5, L10, L15, L20, and L25).

DFT simulations of Raman spectra, using an accurate all-electrons hybrid functional PBE0, fingerprinted the main Raman modes in NZSP identifying spectral regions of impurities. Fig. 3 shows the predicted peak positions (sticks) of

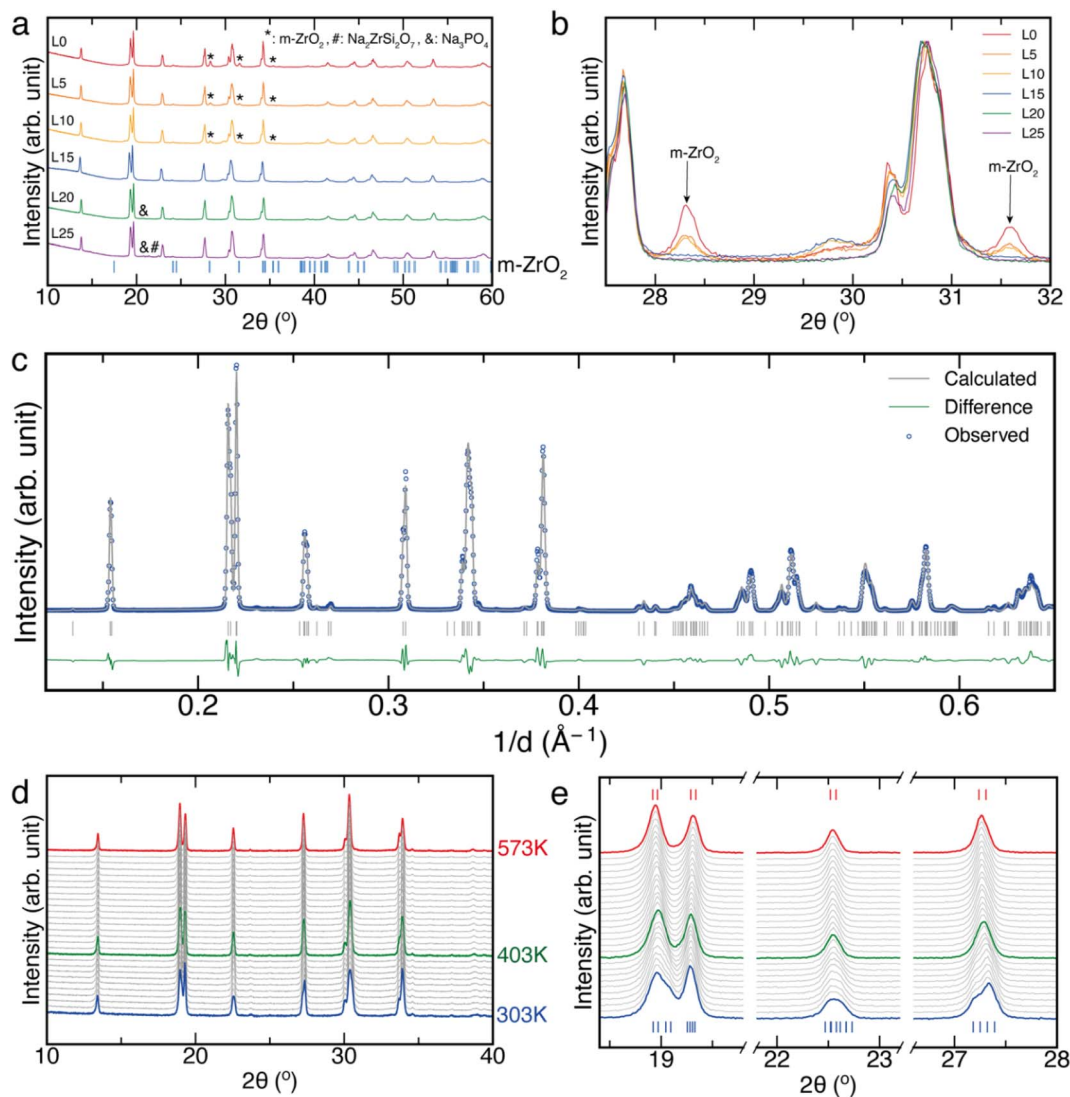


Fig. 2 Powder X-ray diffraction (PXRD) of different sintered pellets of NZSP materials. (a) Shows the laboratory PXRDs of different NZSP pellets synthesized with different content of Zr precursor $\text{ZrO}(\text{NO}_3)_2 \cdot 3.7\text{H}_2\text{O}$. Samples are L0 (–0% $\text{ZrO}(\text{NO}_3)_2 \cdot 3.7\text{H}_2\text{O}$), L5 (–5%), L10 (–10%), L15 (–15%), L20 (–20%), and L25 (–25%). The $m\text{-ZrO}_2$ impurity revealed by PXRD Rietveld refinement is indexed by an asterisk (*), $\text{Na}_2\text{ZrSi}_2\text{O}_7$ by a hash (#), and Na_3PO_4 impurity by an ampersand (&). (b) Shows a decrease of $m\text{-ZrO}_2$ peaks obtained from synthesis, from L0 to L25 in the 2θ -range of 27.5–32.0°. (c) Rietveld refinement of the room temperature (298 K) synchrotron PXRD of sample L15, showing its high purity. (d) Variable temperature PXRD (laboratory) of sample L15 (see also Fig. S5 of ESI†) shown within the temperature range 303–573 K. In panel (e), selected PXRD peaks show the monoclinic-to-rhombohedral phase transformation in the 2θ ranges of 18.6–19.6°, 22–23°, and 26.6–27.8°, noting the key difference in the change of peak intensity, and broadness. The PXRD of 403 K (in green) is better indexed by the rhombohedral ($R\bar{3}c$) NaSICON phase, along with subsequent pattern refinements at higher temperatures.

$\text{Na}_3\text{Zr}_2\text{Si}_2\text{PO}_{12}$ (N3.0ZSP, magenta), $m\text{-ZrO}_2$ (light blue), $\text{Na}_2\text{-ZrSi}_2\text{O}_7$ (maroon), and Na_3PO_4 (black). Although there are some compositional differences between N3.0ZSP and other NZSP compositions, the deviation of the expected peaks is minimal, and hence the computed Raman spectrum N3.0ZSP is used to fingerprint the vibrational modes present in other NZSP compositions (e.g., N3.4ZSP).

The assignment of main Raman peaks detected in experiments was done by inspecting the computed eigenvectors associated with each vibrational mode of the Na, ZrO_6 , SiO_4 , and PO_4 units in NaSICON. Peaks derived from DFT are slightly red-shifted compared to experimental data. $m\text{-ZrO}_2$ peaks are

indexed in Fig. S10† from a zirconia reference measured experimentally.

The most intense peaks in the low-frequency region (between 100 and 600 cm^{-1}) are mostly contributed by: bending modes of ZrO_6 units (red, $\sim 300\text{ cm}^{-1}$) of NaSICONs, stretching modes of ZrO_6 units, and bending modes of SiO_4/PO_4 units (green, $\sim 410\text{ cm}^{-1}$). At higher frequencies (from 800 to 1300 cm^{-1}), stretching modes of SiO_4 and PO_4 units (blue, $\sim 900\text{ cm}^{-1}$, and orange, $\sim 1000\text{ cm}^{-1}$) were identified.

The predicted Raman spectra from DFT reveal that the expected NZSP and impurity peaks are in excellent agreement with the experimental peaks obtained for NZSP and $m\text{-ZrO}_2$. At

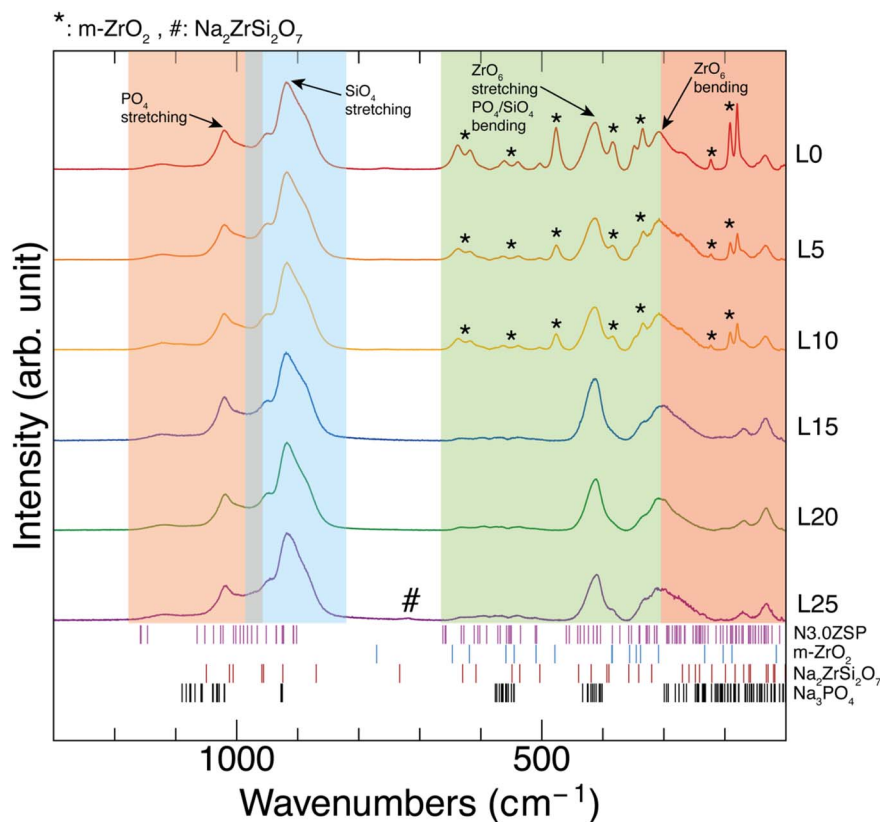


Fig. 3 Raman spectra of the NZSP samples synthesized with different aliquots of Zr precursors. Corresponding phases, as determined by DFT calculations are marked by vertical sticks. Experimental Raman peaks of the impurity phase $m\text{-ZrO}_2$ are marked with *, and $\text{Na}_2\text{ZrSi}_2\text{O}_7$ with #. No distinct peaks correspond to Na_3PO_4 , where the vibrational modes overlap with the NZSP peaks in the spectrum. Raman modes are tabulated in Tables S7–S9 of the ESI.† The red-shaded area ($100\text{--}300\text{ cm}^{-1}$) identifies frequency regions where the resonance of twisting (or “rotation”) of $\text{PO}_4/\text{SiO}_4/\text{ZrO}_6$ and the bending modes of ZrO_6 are found. The green shaded area ($300\text{--}650\text{ cm}^{-1}$) contains mainly the PO_4/SiO_4 bending modes and the ZrO_6 stretching modes. The blue shaded area ($800\text{--}950\text{ cm}^{-1}$) mainly represents the SiO_4 stretching modes, and the orange shaded region ($900\text{--}1300\text{ cm}^{-1}$) the PO_4 stretching modes.

first sight, the Raman spectrum of L15, L20, and L25 shows fewer spectral features than the other L0, L5, and L10 samples – indicating the potential absence of undesired impurities. No peaks corresponding to $m\text{-ZrO}_2$ are visible in the L15, L20, and L25 spectra. In striking contrast, spectra of L0, L5, and L10 manifest clear signatures of $m\text{-ZrO}_2$ (see the green shaded area, from $300\text{ to }650\text{ cm}^{-1}$ of Fig. 3). For L25, there is a small peak at $\sim 730\text{ cm}^{-1}$ corresponding to the $\text{Na}_2\text{ZrSi}_2\text{O}_7$ phase. Na_3PO_4 cannot be clearly detected in both L20 and L25 due to the peaks of Na_3PO_4 overlapping with the NZSP features. This observation reinforces the idea formulated from the PXRD analysis that NZSP synthesis deficient in Zr precursors can reduce or even eliminate (in samples L15, L20, and L25) zirconia as an impurity phase.

SEMs are shown in Fig. 4 together with energy dispersive X-ray spectroscopy (EDS) analysis of L0 and L15 samples. The cross-section was magnified up to $6000\times$, with an accelerating voltage of 10 kV for both imaging and EDS.⁵⁶ The grains, isolated by the boundary detection algorithm,³² show the average grain area of L15 in the sampled cross-section is around $0.093\text{ }\mu\text{m}^2$, with a maximum grain area of $17.18\text{ }\mu\text{m}^2$ and a minimum grain area of $4 \times 10^{-4}\text{ }\mu\text{m}^2$. In Fig. S12 of the ESI,† sample L0

features a less homogeneous grain size distribution with a larger fraction of small grains with areas $<0.1\text{ }\mu\text{m}^2$, but also some very large grains. This suggests that the growth of grains during annealing was greatly hindered by the presence of $m\text{-ZrO}_2$ and introduced significant grain boundaries, which may affect the ionic transport significantly in the pellet.

Fig. 4a and c show the cross-section of the pellet of NZSP L15 and L0, which appear dense and pore-free. EDS analysis (Fig. 4b and d) shows that for sample L15 (Fig. 4b), all elements are evenly distributed in the cross-section, but sample L0 (Fig. 4d) showed obvious localized regions with higher Zr concentration. In accordance with the PXRD findings, these EDS regions of Zr densification can be linked to $m\text{-ZrO}_2$ impurities. Because the $K\alpha$ line of P (2.01 keV) and the $L\alpha$ line of Zr (2.04 keV) appear close to each other,⁵⁶ the P EDS may be a poor representation of the elemental distribution. This may explain why the P EDS also has localized regions that are the same as the Zr EDS in L0. In contrast, in our PXRD and Raman analysis, we did not detect any compound containing Zr and P, other than the main NZSP phase. The morphologies of the pre-sintered powders from L0 to L15 are shown in Fig. S13† (with the areas of the particle size reported in Table S14†). In general, the pre-sintered powders

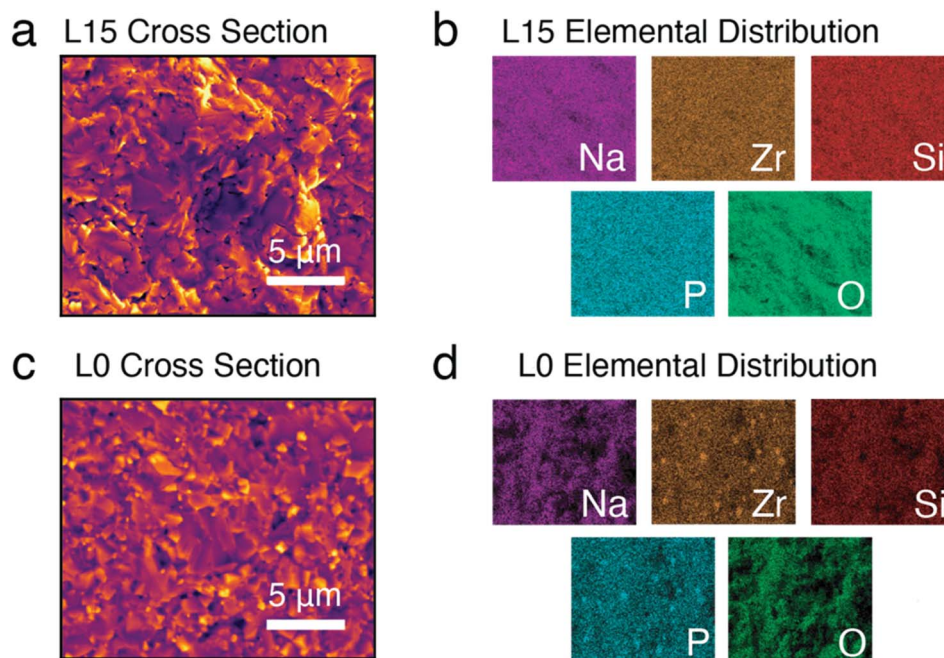


Fig. 4 SEM micrographs and elemental analysis of L0 and L15 samples. Panels (a) and (b) show the SEM and EDS of a cross-section of sample L15. Na, Zr, Si, P, and O appear uniformly distributed in the cross-section of the pellet. Panels (c) and (d) show the SEM and EDS of the cross-section of the L0, revealing the presence of $m\text{-ZrO}_2$ through spots identified in the Zr EDS (panel d). The average grain size as well as the NZSP grains of L0 and L15 are reported in the ESI in Fig. S12.†

display small particle size, which leads to well-sintered pellets with >90% compacity. After considering the weight percentages of the main NZSP phase and the impurity $m\text{-ZrO}_2$ phase, the compacity of the samples L0 and L15 are comparable, at 95.07% and 95.45% respectively.

Using the NZSP pellets of L0 and L15, we now investigate the Na-ion transport using electrochemical impedance spectroscopy (EIS). Fig. 5a and b show Nyquist plots of the L15 pellet at different temperatures. The dimension of the L15 pellet is 7.96 mm in diameter and 2.07 mm in thickness (Nyquist plot and dimensions for sample L0 are given in Fig. S15†). Additionally, we investigate the effect of purity of our NZSP in the cycling performance of $\text{Na}_3\text{V}_2(\text{PO}_4)_3|\text{NZSP-L0}|\text{Na}_3\text{V}_2(\text{PO}_4)_3$ and $\text{Na}_3\text{V}_2(\text{PO}_4)_3|\text{NZSP-L15}|\text{Na}_3\text{V}_2(\text{PO}_4)_3$ symmetric cells, the initial specific capacities at different C rates, and the polarization reported in Fig. S16 and Table S17 in the ESI.† Note, $\text{Na}_{1+x}\text{V}_2(\text{PO}_4)_3$ can be used ambivalently as the positive and negative electrode. Expectedly, the specific capacity of the L15 symmetric cell at different C rates (C/20, C/10, and C/5) is consistently higher than that of the symmetric cell using the ZrO_2 -contaminated L0 as the solid electrolyte. The specific capacity of L15 at C/20, C/10 and C/5 rate saw an initial charge capacity of $\sim 91.94 \text{ mA h g}^{-1}$, $\sim 57.90 \text{ mA h g}^{-1}$, and $\sim 17.31 \text{ mA h g}^{-1}$ respectively, whereas the specific capacity of L0 at the same rates saw an initial capacity of $\sim 61.49 \text{ mA h g}^{-1}$, $\sim 30.01 \text{ mA h g}^{-1}$, and $\sim 4.70 \text{ mA h g}^{-1}$, respectively. The L0-based symmetric cell also experiences a larger polarization compared to the analogue L15 cell. At C/20, C/10, and C/5 rates, the polarization value of the L15 symmetric cell is 0.62 V, 1.27 V, and 1.63 V respectively, while the polarization of the L0 symmetric cell for the same C-

rates is 1.31 V, 1.50 V, and 2.22 V. The presence of $m\text{-ZrO}_2$ hinders the charge/discharge profile lowering the specific capacity and contributing to an increase of the cell polarization. These results highlight the importance of having a zirconia-free solid electrolyte layer in a Na-ion all-solid-state battery. Photographs of the sputter L15 pellet, along with the full cell of NVP|L15|NVP setup up is shown in Fig. S18 of the ESI.†

The equivalent circuits used for interpreting EIS measurements are in Fig. 5a and b. Ionic conductivities were measured at 173 K to 573 K, with a 20 K heating step. The soaking time was 15 minutes before each measurement. Low-temperature measurements are crucial to separate the bulk resistance from the grain-boundary resistance. Fig. 5a shows the Nyquist of 193 K of L15, which can resolve the impedance envelope into two main features: (i) at high to moderate frequencies – the bulk conductivity of sample L15, and (ii) at moderate to lower frequencies – the grain boundary resistance of L15.

The Nyquist plot obtained for L15 at 193 K in Fig. 5a shows two distinct semicircles and a diffusion tail: a smaller semicircle at higher frequencies, a larger semicircle at moderate to lower frequencies, followed by a semi-infinite linear diffusion line at lower frequencies. The smaller semicircle in the Nyquist plot associated with a capacitance of about 30 pF represents the charge transfer process happening in parallel with the geometric capacitance of the bulk, while the larger semicircle (with a 140 times larger capacitance) represents the same charge transfer process and parallel capacitance at grain boundaries. The equivalent circuit used to model the Nyquist plot was the following: resistor R1 representing the cable and contact resistances, R2 in parallel to Constant Phase Element

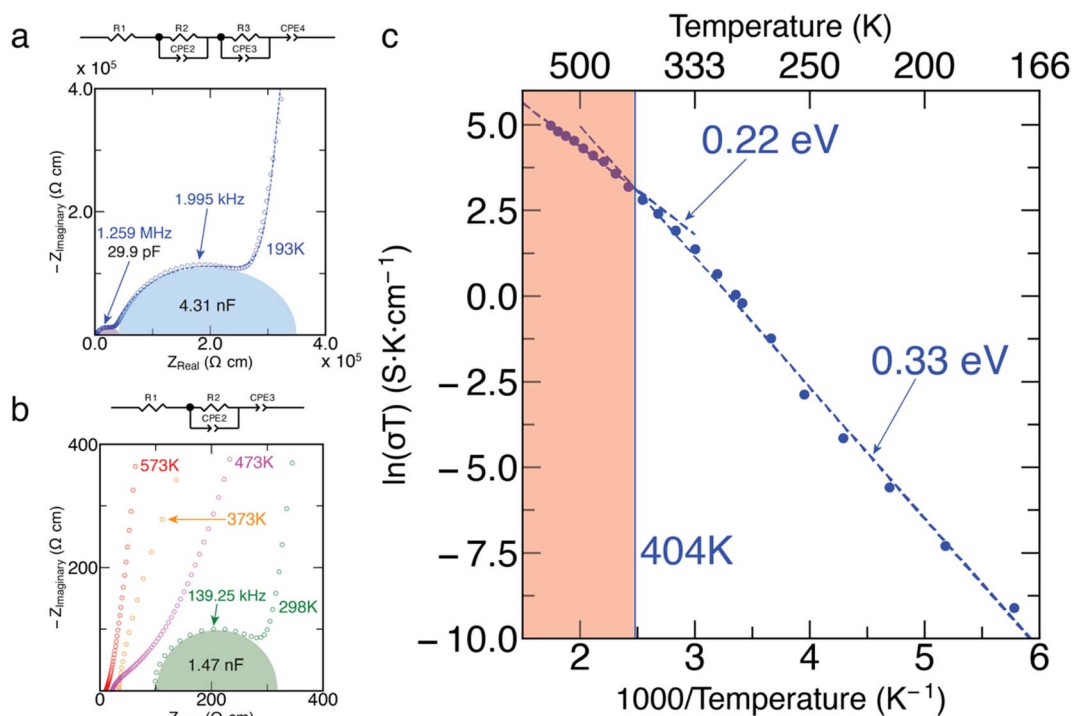


Fig. 5 Electrochemical impedance spectroscopy of the L15 NZSP sample, and equivalent circuits used for fitting. (a) Nyquist plot of sample L15 at 193 K, where two semicircles are observed. The smaller semicircle at high to moderate frequencies is the impedance of the bulk phase. The larger semicircle at moderate to lower frequencies is the grain boundary resistance. Fitted curves are shown by dashed lines. Because of the presence of two semicircles, the associated equivalence circuit used to model the Nyquist plot has 2 sets of resistors (R) and Constant Phase Element (CPE) in parallel, while a resistor (R1) accounts for the cable and contact resistances. (b) Nyquist plot of L15 at moderate to high temperatures. As the measurement in (b) can only detect a single depressed semicircle, a simpler equivalent circuit, consisting of only one resistor and CPE in parallel, was used. The total ionic conductivity at 298 K was determined to be $\sim 3.49 \text{ mS cm}^{-1}$. (c) The Arrhenius plot of sample L15 in the temperature range from 173 K to 573 K. Derived activation energies are $\sim 0.33 \text{ eV}$ for the low-temperature monoclinic phase and $\sim 0.22 \text{ eV}$ for the high-temperature rhombohedral phase $> 404 \text{ K}$. The transition temperature obtained from the Arrhenius plot is $\sim 404 \text{ K}$, above which the NZSP exists in the rhombohedral phase (orange-shade).

CPE2 for the resistance and pseudo-capacitance for the small semicircle observed at high frequencies, R3 in parallel to CPE3 for the larger semicircle at moderate to low frequencies, and CPE4 representing the semi-infinite diffusion tail. Using these equivalent circuits, the total conductivity determined for sample L15 at 193 K is $\sim 3.38 \pm 0.01 \mu\text{S cm}^{-1}$, with a bulk ionic conductivity of $\sim 41 \pm 2 \mu\text{S cm}^{-1}$. Details of the fit of L15 at 193 K in Fig. 5a are reported in Table S19 of the ESI.†

For increasing temperatures in the range $193 \text{ K} < T < 573 \text{ K}$ ($\sim 300^\circ\text{C}$), the semicircles in the Nyquist plots shift to higher frequencies as Na-ion transport experiences lower resistance demonstrated by the disappearance of the bulk envelope in Fig. 5b. At moderate to high temperatures, the EIS measurements for the same frequency window present a single depressed semicircle followed by a diffusion tail at lower frequencies, requiring a simpler equivalent circuit to fit Fig. 5b. The circuit used for Fig. 5b consists of a resistor (R1) modeling the bulk resistance (in this case indistinguishable with the relatively small contact resistances), R2 in parallel to CPE2 to model the charge transfer at grain boundaries at higher frequencies, and a CPE3 capturing the semi-infinite diffusion tail at lower frequencies.

At room temperature (298 K), the measured total conductivity for sample L15 is $3.49 \pm 0.08 \text{ mS cm}^{-1}$, comparable but

slightly lower compared to measurements of N3.4ZSP in an earlier study (4.48 mS cm^{-1}).³² The bulk conductivity of the L15 sample is approximately $10.1 \pm 0.2 \text{ mS cm}^{-1}$, which agrees well with values reported elsewhere for N3.4ZSP.³² The electronic transference number was determined to be 1.57×10^{-5} , as shown in Fig. S20 in the ESI.† The low electronic conductivity shows that the conductivity of sample L15 is strictly ionic.

To verify the effect of impurity phases, in this case, m-ZrO₂, on the ionic conductivity of NZSP, we also conducted low-temperature impedance measurements of the NZSP L0 pellet. The Nyquist plot for the EIS spectrum of L0 at 193 K, as well as the equivalent circuit used to fit it can be found in Fig. S15,† while showing a comparison between L0 and L15 Nyquist plots at 193 K. Due to the significant amount of m-ZrO₂ present in L0 ($\sim 8\%$ according to PXRD measurements), the equivalent circuit used to model L0 is more complex than that of L15, requiring more elements to fit contributions arising from impurities in the sample. The fitted values are reported in Table S21 of ESI.† The measured total conductivity at 193 K is $25.25 \pm 0.09 \text{ nS cm}^{-1}$, and the bulk conductivity extracted is $\sim 31 \pm 3 \mu\text{S cm}^{-1}$. While the bulk conductivity is comparable to that of L15 ($\sim 41 \pm 2 \mu\text{S cm}^{-1}$), the total conductivity for L0 is two orders of magnitude lower compared to that of L15 ($\sim 3.38 \pm$

$0.01 \mu\text{S cm}^{-1}$), highlighting that the substantial amount of m-ZrO₂ greatly affects the ion transport within the NZSP pellet. Similarly, we expect both L5 and L10 samples to have total ionic conductivity between L0 and L15, while having similar bulk ionic conductivity values as m-ZrO₂ affects only the total Na⁺ conductivity.

The reason why there may be such a low ionic conductivity may be due to the size of the synthesized batch. As the synthesis batch is relatively small (1–2 g per synthesis), we must expect some impact of evaporation of Na and/or P leading to stoichiometry deviations including an excess of Zr. This leads to a high m-ZrO₂ content in L0. A viable solution is to synthesize NZSP in larger batches (e.g., 50 g per batch), where the impact of the Na and P evaporation can be curbed compared to the syntheses reported here.

Arrhenius plot of Fig. 5c was obtained from the variable temperature impedance data of sample L15. Two distinct regimes can be identified: the low-temperature monoclinic phase with a migration energy of ~ 0.33 eV, followed by a lower migration energy of ~ 0.22 eV for the high-temperature rhombohedral phase. The transition temperature determined is $\sim 404 \pm 9$ K and agrees well with the DSC data obtained (~ 396.5 K), as well as the transition temperature derived from variable temperature XRD (~ 403 K).

Discussion

Here, we proposed an effective synthesis protocol based on the solution-assisted method to reduce, if not eliminate, the m-ZrO₂ impurity in NZSP solid electrolytes. The absence of m-ZrO₂ provides significant increase in Na-ion conductivities, showcasing the importance of this study. We also concentrated on the composition Na_{3.4}Zr_{1.71}Si_{2.41}P_{0.59}O_{11.42} which shows the most promising Na-ion conductivities.^{21,32} In practice, our strategy to obtain zirconia-free NZSPs hinges on subsequent reductions of the amount of Zr precursors used in the solution-assisted method and is general to the synthesis of all NZSP compositions. Through a synthesis carried out in a deficiency of Zr precursor (*i.e.* using only 85% of stoichiometric ZrO(NO₃)₂·3.7H₂O), we achieved a zirconia-free NZSP material. We ascertained the absence of undesired impurities using a combination of synchrotron powder X-ray diffraction (PXRD) and Raman spectroscopy, which verifies the absence of impurities from any amorphous phase. While having Zr deficient stoichiometry may result in Zr deficient NZSP compositions, X-ray diffractions show that the main NZSP phase is still detected. It is also of paramount importance to explain the connection of sample purity with measured ionic conductivity. Therefore, we put forward three hypotheses to explain why the PXRD patterns can still be indexed by Na_{3.4}Zr_{1.71}Si_{2.41}P_{0.59}O_{11.42} even in the regime of off-stoichiometry for the Zr precursor, and link these differences to ionic conductivities recorded.

(1) The synthesized NZSP phase may be Zr deficient. However, the crystal structure determined from Rietveld refinement of the PXRD still matches closely with the N3.4ZSP structure. The ICP-OES result seems to suggest a Zr deficient NZSP that is partially charge compensated by Na, and possibly

charge compensated through appropriate reduction of O, which may lead to a Von Alpen-type NaSICON^{33,51} phase such as Na_{3.4}Zr_{1.71}Si_{2.41}P_{0.59}O_{11.42}.

(2) A Zr deficient stoichiometry in L15 results in NZSP with a composition that is close to the nominal composition of N3.4ZSP while the excess Na/P/Si precursors form amorphous silicate (essentially amorphous Na₂SiO₃) and to a lesser extent phosphate glasses that remain undetectable by X-ray (due to their limited amount and amorphous nature) and by Raman (due to the small amount and overlap of their Raman bands with those of the dominating NZSP phase). The effect of amorphous Na₂SiO₃ will cause the total Na-ionic conductivity of the NZSP solid electrolyte to decrease. As substantiated by recent studies,^{57,58} a high amount of Na₂SiO₃ can result in a decrease in ionic conductivity, explained by the formation of impurities such as Na₂ZrSi₂O₇ and Na₃PO₄. SEMs demonstrated low porosity of the L15 sample consistent with the high compacity (95.45%), which may indicate a low fraction of the amorphous phase in the NZSP sample that is undetectable with XRD or Raman.

(3) A NZSP pellet was synthesized that may give rise to a stoichiometry that is not close to the nominal composition of N3.4ZSP, with a distinct composition, but having a similar crystal structure that can be understood as a defect variant of the N3.4ZSP structure. There have been claims of various types of NaSICONs,⁵³ with complex formulae, such as Na_{1+4y+x}Zr_{2-y-z}Si_xP_{3-x}O_{12-2z}, based on off-stoichiometric phases of the quaternary phase space Na₂O–P₂O₅–SiO₂–ZrO₂. Here the overall sodium content can be charge-compensated by adjustments of the Si : P ratio, Zr and/or oxygen deficiencies. Our NZSP samples could adopt one such chemical composition, Na_{3.63}Zr_{1.71}Si_{2.41}P_{0.59}O_{11.53}, exactly in line with the ICP-OES result.

Although we cannot pinpoint the exact defect structure of the NZSP samples here, it is demonstrated that an appropriate dosage of the Zr precursor is required to enable the synthesis of a favorably high grain boundary conductivity due to the absence of crystalline impurity phases. Certainly, discerning between nominal composition and real composition remains an important challenge for this field. A practical strategy to ensure an accurate ratio of reagents entails a quantitative and phase-sensitive determination of their composition as well as a quantitative monitoring of any evaporation processes during the high-temperature processing through mass spectrometry or comparable elemental analyses.⁵⁹

Conclusion

In summary, we achieved the synthesis of zirconia-free NZSP by appropriately varying the amount of Zr precursors. Through Rietveld analysis of synchrotron powder X-ray diffractions, we confirmed that reducing the nominal Zr content by 15% leads to zirconia-free NZSP samples. Raman spectroscopy results not only corroborated these findings but also suggested the absence of significant amounts of any crystalline or amorphous impurity phase other than NaSICON-type NZSP. The removal of zirconia impurities increased the low-temperature (at 193 K) Na-ion total conductivity *via* two orders of magnitude increase in grain

boundaries conductivity. These results provide an important protocol for the synthesis of phase-pure NASICON materials for a rational design of electrolytes and electrode materials for secondary batteries, including all-solid-state batteries.

Conflicts of interest

There are no conflicts to declare.

Acknowledgements

A. J. K. T., Y. L., P. C., S. A., E. M., C. M., V. S., and J.-N. C. are grateful to the ANR-NRF for the funding of the NRF2019-NRF-ANR073 Na-MASTER project. P. C. and Z. D. acknowledge funding from the National Research Foundation under NRF Fellowship NRFF12-2020-0012. Z. D. acknowledges the support from his Lee Kuan Yew Postdoctoral Fellowship 22-5930-A0001. The computational work was performed on resources of the National Supercomputing Centre, Singapore (<https://www.nscc.sg>).

References

- 1 J. Goodenough, How we made the Li-ion rechargeable battery, *Nat. Electron.*, 2018, **1**(3), 204.
- 2 A. Ponrouch, E. Marchante, M. Courty, J.-M. Tarascon and M. R. Palacin, In search of an optimized electrolyte for Na-ion batteries, *Energy Environ. Sci.*, 2012, **5**(9), 8572.
- 3 Q. Li, J. Chen, L. Fan, X. Kong and Y. Lu, Progress in electrolytes for rechargeable Li-based batteries and beyond, *Green Energy Environ.*, 2016, **1**(1), 18–42.
- 4 A. Jana, R. Paul and A. Roy, Architectural design and promises of carbon materials for energy conversion and storage: in laboratory and industry, *Carbon Based Nanomaterials for Advanced Thermal and Electrochemical Energy Storage and Conversion*, 2019, pp. 25–61.
- 5 A. A. Yaroshevsky, Abundances of chemical elements in the Earth's crust, *Geochem. Int.*, 2006, **44**(1), 48–55.
- 6 T. Famprikis, P. Canepa, J. Dawson, M. Islam and C. Masquelier, Fundamentals of inorganic solid-state electrolytes for batteries, *Nat. Mater.*, 2019, **18**(12), 1278–1291.
- 7 C. Li, *et al.*, NASICON: a promising solid electrolyte for solid-state sodium batteries, *Interdiscip. Mater.*, 2022, **1**(3), 396–416.
- 8 M. Guin and F. Tietz, Survey of the transport properties of sodium superionic conductor materials for use in sodium batteries, *J. Power Sources*, 2015, **273**, 1056–1064.
- 9 Y. Liu, *et al.*, A niobium-substituted sodium superionic conductor with conductivity higher than 5.5 mS cm⁻¹ prepared by solution-assisted solid-state reaction method, *J. Power Sources*, 2022, **518**, 230765.
- 10 F. Stainer, B. Gadermaier, A. Kugerl, L. Ladenstein, K. Hogrefe and H. M. Wilkening, Fast Na⁺ ion dynamics in the Nb⁵⁺ bearing NASICON Na_{3+x-z}Nb_zZr_{2-z}Si_{2+x}P_{1-x}O₁₂ as probed by ²³Na NMR and conductivity spectroscopy, *Solid State Ionics*, 2023, **395**, 116209.
- 11 Y. Deng, *et al.*, Crystal Structures, local atomic environments, and ion diffusion mechanisms of scandium-substituted sodium superionic conductor (NASICON) solid electrolytes, *Chem. Mater.*, 2018, **30**(8), 2618–2630.
- 12 Q. Ma, *et al.*, Scandium-substituted Na₃Zr₂(SiO₄)₂(PO₄) prepared by a solution-assisted solid-state reaction method as sodium-ion conductors, *Chem. Mater.*, 2016, **28**(13), 4821–4828.
- 13 K. Saravanan, C. Mason, A. Rudola, K. Wong and P. Balaya, The First Report on Excellent Cycling Stability and Superior Rate Capability of Na₃V₂(PO₄)₃ for Sodium Ion Batteries, *Adv. Energy Mater.*, 2012, **3**(4), 444–450.
- 14 B. Singh, *et al.*, A chemical map of NASICON electrode materials for sodium-ion batteries, *J. Mater. Chem. A*, 2021, **9**(1), 281–292.
- 15 C. Delmas, F. Cherkaoui, A. Nadiri and P. Hagenmuller, A NASICON-type phase as intercalation electrode: NaTi₂(PO₄)₃, *Mater. Res. Bull.*, 1987, **22**(5), 631–639.
- 16 N. R. Khasanova, *et al.*, NaNbV(PO₄)₃: Multielectron NASICON-type anode material for Na-ion batteries with excellent rate capability, *ACS Appl. Mater. Interfaces*, 2023, **15**(25), 30272–30280.
- 17 A. K. Paidi, *et al.*, Na₂ZrFe(PO₄)₃ – a rhombohedral NASICON-structured material: Synthesis, structure and Na-intercalation behavior, *Inorg. Chem.*, 2023, **62**(10), 4124–4135.
- 18 B. Patra, *et al.*, Unveiling a high capacity multi-redox (Nb⁵⁺/Nb⁴⁺/Nb³⁺) NASICON-Nb₂(PO₄)₃ anode for Li- and Na-Ion Batteries, *J. Mater. Chem. A*, 2023, **11**(15), 8173–8183.
- 19 J. Wang, *et al.*, A high-energy NASICON-type cathode material for Na-Ion Batteries, *Adv. Energy Mater.*, 2020, **10**(10), 1903968.
- 20 J. Pereira da Silva, *et al.*, Sintering of a sodium-based NASICON electrolyte: A comparative study between cold, field assisted and conventional sintering methods, *J. Eur. Ceram. Soc.*, 2019, **39**(8), 2697–2702.
- 21 Q. Ma, C. Tsai, X. Wei, M. Heggen, F. Tietz and J. Irvine, Room temperature demonstration of a sodium superionic conductor with grain conductivity in excess of 0.01 S cm⁻¹ and its primary applications in symmetric battery cells, *J. Mater. Chem. A*, 2019, **7**(13), 7766–7776.
- 22 Z. Jian, Y. Hu, X. Ji and W. Chen, NASICON-Structured Materials for Energy Storage, *Adv. Mater.*, 2017, **29**(20), 1601925.
- 23 Z. Deng, *et al.*, Phase Behavior in Rhombohedral NaSiCON Electrolytes and Electrodes, *Chem. Mater.*, 2020, **32**(18), 7908–7920.
- 24 A. Chakraborty, R. Thirupathi, S. Bhattacharyya, K. Singh and S. Omar, Mg-doped NASICON-type electrolyte for rechargeable solid-state sodium-ion batteries, *J. Power Sources*, 2023, **572**, 233092.
- 25 C. Wen, *et al.*, Enhanced electrochemical properties of NASICON-Type Na₃Zr₂Si₂PO₁₂ solid electrolytes with Tb³⁺-ions-assisted sintering, *Solid State Ionics*, 2023, **393**, 116185.
- 26 B. Ouyang, *et al.*, Synthetic accessibility and stability rules of NASICONs, *Nat. Commun.*, 2021, **12**(1), 5752.
- 27 J. Goodenough, H. Hong and J. Kafalas, Fast Na⁺-ion transport in skeleton structures, *Mater. Res. Bull.*, 1976, **11**(2), 203–220.

- 28 H. Hong, Crystal structures and crystal chemistry in the system $\text{Na}_{1+x}\text{Zr}_2\text{Si}_x\text{P}_{3-x}\text{O}_{12}$, *Mater. Res. Bull.*, 1976, **11**(2), 173–182.
- 29 A. G. Jolley, D. D. Taylor, N. J. Schreiber and E. D. Wachsman, Structural investigation of monoclinic-rhombohedral phase transition in $\text{Na}_3\text{Zr}_2\text{Si}_2\text{PO}_{12}$ and doped NASICON, *J. Am. Ceram. Soc.*, 2015, **98**(9), 2902–2907.
- 30 H. Park, K. Jung, M. Nezafati, C.-S. Kim and B. Kang, Sodium ion diffusion in NASICON ($\text{Na}_3\text{Zr}_2\text{Si}_2\text{PO}_{12}$) solid electrolytes: Effects of excess sodium, *ACS Appl. Mater. Interfaces*, 2016, **8**(41), 27814–27824.
- 31 Z. Zhang, *et al.*, A self-forming composite electrolyte for solid-state sodium battery with ultralong cycle life, *Adv. Energy Mater.*, 2016, **7**(4), 1601196.
- 32 Z. Deng, T. P. Mishra, E. Mahayoni, Q. Ma, A. J. K. Tieu, O. Guillon, J.-N. Chotard, V. Seznec, A. K. Cheetham, C. Masquelier, G. S. Gautam and P. Canepa, Fundamental investigations on the sodium-ion transport properties of mixed polyanion solid-state battery electrolytes, *Nat. Commun.*, 2022, **13**(1), 4470.
- 33 U. Von Alpen, M. Bell and H. Hofer, Compositional dependence of the electrochemical and structural parameters in the NASICON system ($\text{Na}_{1+x}\text{Si}_x\text{Zr}_{2-x}\text{P}_{3-x}\text{O}_{12}$), *Solid State Ionics*, 1981, **3–4**, 215–218.
- 34 P. K. Jha, O. P. Pandey and K. Singh, Optimization of high conducting $\text{Na}_3\text{Zr}_2\text{Si}_2\text{PO}_{12}$ phase by new phosphate salt for solid electrolyte, *Silicon*, 2016, **9**(3), 411–419.
- 35 Y. Li, Z. Sun, C. Sun, H. Jin and Y. Zhao, Exploring the origin of ZrO_2 phase in $\text{Na}_3\text{Zr}_2\text{Si}_2\text{PO}_{12}$ ceramic electrolyte, *Ceram. Int.*, 2023, **49**(2), 3094–3098.
- 36 Y. Shimizu, Y. Azuma and S. Michishita, Sol–gel synthesis of NASICON discs from aqueous solution, *J. Mater. Chem.*, 1997, **7**(8), 1457–1460.
- 37 Y. Li and M. Xie, Sodium-ion solid-state electrolyte, *ACS Symposium Series*, 2022, pp. 275–294.
- 38 K. Singh, A. Chakraborty, R. Thirupathi and S. Omar, Recent advances in NASICON-type oxide electrolytes for solid-state sodium-ion rechargeable batteries, *Ionics*, 2022, **28**(12), 5289–5319.
- 39 L. Zhang, Y. Liu, Y. You, A. Vinu and L. Mai, NASICONs-type solid-state electrolytes: the history, physicochemical properties, and challenges, *Interdiscip. Mater.*, 2022, **2**(1), 91–110.
- 40 Z. Sun, Y. Li, M. Liu, H. Jin and Y. Zhao, Screening of sintering AIDs for Oxide Ceramics: A case of NASICON electrolyte, *Small*, 2023, **19**(33), 2301230.
- 41 J.-S. Lee, C.-M. Chang, Y. I. L. Lee, J.-H. Lee and S.-H. Hong, Spark plasma sintering (SPS) of NASICON Ceramics, *J. Am. Ceram. Soc.*, 2004, **87**(2), 305–307.
- 42 S. Narayanan, S. Reid, S. Butler and V. Thangadurai, Sintering temperature, excess sodium, and phosphorous dependencies on morphology and ionic conductivity of NASICON $\text{Na}_3\text{Zr}_2\text{Si}_2\text{PO}_{12}$, *Solid State Ionics*, 2019, **331**, 22–29.
- 43 S. Naqash, Q. Ma, F. Tietz and O. Guillon, $\text{Na}_3\text{Zr}_2(\text{SiO}_4)_2(\text{PO}_4)$ prepared by a solution-assisted solid state reaction, *Solid State Ionics*, 2017, **302**, 83–91.
- 44 A. Jalalian-Khakshour, *et al.*, Solid-state synthesis of NASICON ($\text{Na}_3\text{Zr}_2\text{Si}_2\text{PO}_{12}$) using nanoparticle precursors for optimisation of ionic conductivity, *J. Mater. Sci.*, 2019, **55**(6), 2291–2302.
- 45 S. Narayanan, S. Reid, S. Butler and V. Thangadurai, Sintering temperature, excess sodium, and phosphorous dependencies on morphology and ionic conductivity of NASICON $\text{Na}_3\text{Zr}_2\text{Si}_2\text{PO}_{12}$, *Solid State Ionics*, 2019, **331**, 22–29.
- 46 B. Santhoshkumar, *et al.*, Improved ionic conductivity of $\text{Na}_{3+x}\text{Sc}_x\text{Zr}_{2-x}\text{Si}_2\text{PO}_{12}$ ($x = 0.2, 0.3, 0.4, 0.5$) NASICON via optimized sintering conditions: investigation of crystal structure, local atomic structure, and microstructure, *Chem. Phys. Lett.*, 2021, **776**, 138706.
- 47 M. Guin, *et al.*, Stability of NASICON materials against water and CO_2 uptake, *Solid State Ionics*, 2017, **302**, 102–106.
- 48 R. Fuentes, Reaction of NASICON with water, *Solid State Ionics*, 2001, **139**(3–4), 309–314.
- 49 T. Kida, K. Shimanoe, N. Miura and N. Yamazoe, Stability of NASICON-based CO_2 sensor under humid conditions at low temperature, *Sens. Actuators, B*, 2001, **75**(3), 179–187.
- 50 N. Anantharamulu, *et al.*, A wide-ranging review on NASICON type materials, *J. Mater. Sci.*, 2011, **46**(9), 2821–2837.
- 51 J. M. Valle, *et al.*, Characterization of hot-pressed Von Alpen type NASICON ceramic electrolytes, *Solid State Ionics*, 2021, **369**, 115712.
- 52 J. P. Boilot, G. Collin and R. Comes, Zirconium deficiency in NASICON-type compounds: Crystal structure of $\text{Na}_5\text{Zr}(\text{PO}_4)_3$, *J. Solid State Chem.*, 1983, **50**(1), 91–99.
- 53 F. Tietz, Phase relations of NASICON materials and compilation of the quaternary phase diagram $\text{Na}_2\text{O-P}_2\text{O}_5\text{-SiO}_2\text{-ZrO}_2$, *AIMS Mater. Sci.*, 2017, **4**(6), 1305–1318.
- 54 X. Wang, J. Chen, D. Wang and Z. Mao, Improving the alkali metal electrode/inorganic solid electrolyte contact via room-temperature ultrasound solid welding, *Nat. Commun.*, 2021, **12**(1), 7109.
- 55 M. K. Chong, Z. Zainuddin, F. S. Omar and M. H. Jumali, $\text{Na}_3\text{Zr}_2\text{Si}_2\text{PO}_{12}$ NASICON-type solid electrolyte: influence of milling duration on microstructure and ionic conductivity mechanism, *Ceram. Int.*, 2022, **48**(15), 22106–22113.
- 56 *K X-Ray Data Booklet, Table 1-2*, Lawrence Berkeley National Laboratory.
- 57 J. A. Oh, *et al.*, Composite NASICON ($\text{Na}_3\text{Zr}_2\text{Si}_2\text{PO}_{12}$) solid-state electrolyte with enhanced Na^+ ionic conductivity: effect of liquid phase sintering, *ACS Appl. Mater. Interfaces*, 2019, **11**(43), 40125–40133.
- 58 H. Wang, *et al.*, Enhanced ionic conductivity of a $\text{Na}_3\text{Zr}_2\text{Si}_2\text{PO}_{12}$ solid electrolyte with Na_2SiO_3 obtained by Liquid Phase Sintering for solid-state Na^+ batteries, *Nanoscale*, 2022, **14**(3), 823–832.
- 59 Ö. U. Kudu, *et al.*, Structural details in Li_3PS_4 : variety in thiophosphate building blocks and correlation to Ion Transport, *Energy Storage Mater.*, 2022, **44**, 168–179.